Stall/Post-Stall Modeling
of the Longitudinal Characteristics
# of a General Aviation Aircraft

Gavin K. Ananda[*] and Michael S. Selig[†]

Department of Aerospace Engineering, University of Illinois at Urbana–Champaign, Urbana, IL 61801, USA

The high rate of accidents in general aviation due to pilot loss of control has necessitated the need to find better methods of training pilots. Pilot control and awareness in the stall/post-stall regime can be improved through the use of higher fidelity flight simulators. To create a high fidelity aerodynamic model in the stall/post-stall regime to be implemented in a flight simulator, both steady and unsteady aircraft characteristics need to be represented. In this paper, the detailed development of a steady-state high-angle-of-attack general aviation aircraft longitudinal aerodynamic model is described. The steady-state model uses a component buildup approach that uses strip theory to output the aerodynamic forces and moments of an aircraft. An integrated non-linear lifting-line theory approach is used to model the wing and horizontal tail. Longitudinal effects due to elevator deflections are also included. Validation studies are performed against static wind tunnel datasets for a typical single-engine low-wing general aviation aircraft design.

Nomenclature

A	=	fuselage cross-sectional area
A_b	=	fuselage base area (at $x = l$)
A_p	=	fuselage planform area for most cases
A_r	=	fuselage reference area (taken as A_b)
$\mathit{\!R}$	=	aspect ratio
b	=	wingspan
b_0	=	cross-section width
c	=	chord
$C_{F_{A_{SF}}}$	=	fuselage surface skin friction coefficient
c_f	=	flap chord
C_d	=	airfoil drag coefficient
C_{d_n}	=	crossflow drag coefficient of circular cylinder section
C_D	=	surface drag coefficient ($= D/\frac{1}{2}\rho V_\infty^2 S_{ref}$)
C_l	=	airfoil lift coefficient
$C_{l\alpha}$	=	airfoil lift curve slope
$C_{l_{max}}$	=	airfoil maximum lift coefficient
C_L	=	surface lift coefficient ($= L/\frac{1}{2}\rho V_\infty^2 S_{ref}$)
$C_{m_{c/4}}$	=	airfoil moment coefficient at quarter chord
$C_{M_{c/4}}$	=	surface moment coefficient at quarter chord ($= M/\frac{1}{2}\rho V_\infty^2 S_{ref}c$)
C_N	=	surface normal force coefficient ($= N/\frac{1}{2}\rho V_\infty^2 S_{ref}$)
C_n	=	local normal-force coefficient per unit length

---

*Graduate Student (Ph.D. Candidate), 104 S. Wright St., AIAA Student Member. anandak1@illinois.edu
†Professor, 104 S. Wright St., AIAA Associate Fellow. m-selig@illinois.edu

American Institute of Aeronautics and Astronautics

d_F	=	fuselage cross-section diameter
D	=	drag
D_{ind}	=	induced drag
k	=	corner radius
l_{ref}	=	reference length
l_F	=	fuselage length
L	=	lift
M	=	moment
n_P	=	number of lifting surface panels
N	=	normal force
r_F	=	fuselage cross-section radius
Re	=	Reynolds number based on mean aerodynamic chord ($= V_\infty c/\nu$)
S	=	lifting surface area
S_f	=	flap area
S_{ref}	=	reference area
V_∞	=	freestream velocity
V_F	=	fuselage volume
w_{ind}	=	velocity induced by shed vortices
V_{rel}	=	relative velocity
w_F	=	fuselage width
x_F	=	axial distance from fuselage nose
x_{ac_F}	=	distance from nose to aerodynamic center of fuselage
x_{c_F}	=	distance from nose to centroid of fuselage planform area
x_{m_F}	=	distance from nose to centroid of fuselage pitching-moment reference center
x_{PS}, y_{PS}, z_{PS}	=	location of spanwise panel station points
$x_{LLT}, y_{LLT}, z_{LLT}$ =		location of lifting-line points
Y	=	side force
α_{eff}	=	effective angle of attack
α_{geo}	=	geometric angle of attack
α_{ind}	=	induced angle of attack
β	=	sideslip angle
δ_f	=	flap deflection angle
η	=	flap effectiveness correction factor
η_{fuse}	=	fuselage crossflow drag proportionality factor
Γ	=	circulation
Γ_0	=	circulation at center-span
Γ_{LLT}	=	circulation at the lifting-line points
Γ_{SV}	=	shed vortex circulation
τ	=	flap effectiveness factor
θ_f	=	factor relating flap to chord ratio to flap effectiveness factor
ν	=	kinematic viscosity
ρ	=	density of air

Subscripts

$c/4$	=	quarter-chord
cy	=	cylinder
CF	=	cross-flow
F	=	fuselage
$Newt$	=	Newtonian theory
o	=	equivalent circular body of cross section
SB	=	slender body

I. Introduction

The need to improve air safety has always been at the forefront of the airline and transportation industry. The Colgan Air 3407 and Air France Flight 447 accidents[1,2] that occurred in February and June 2009, respectively, highlighted deficiencies in pilot training with respect to recovering the aircraft from stall and upset states. Furthermore, a recently-concluded 16 year study by Calspan,[3] funded mainly by NASA, the Federal Aviation Administration (FAA), and the United States Navy, concluded that pilots were ill-equipped and untrained to recognize an aircraft in an upset state and then perform any appropriate control inputs to successfully recover from this state.

As a result, the FAA and the European Aviation Safety Agency proposed new rules[4–6] concerning the use of enhanced Flight Simulation Training Devices (FSTD) for special hazard training such as loss of control. The rulings set a five year mandatory compliance deadline (ending in 2018) to FSTD manufacturers for the proper modeling of stall and upset recovery situations, and that they be valid for at least 10 deg beyond the stall angle of attack. At present, research is being conducted into the improvement of commercial transport aircraft flight modeling and control through the NASA Aviation Safety and Security Program (AvSSP)[7–11] and the European Union Simulation and Upset Recovery in Aviation project.[12–16]

The importance attached to commercial transport aircraft is understandable given that passenger safety is of the utmost importance to the transportation industry. However, according to the Aircraft Owners and Pilots Association Air Safety Institute 2010 Nall Report,[17] for fixed wing aircraft over the past decade, the average accident rate was 67% higher for non-commercial flights and the rate of fatal accidents was 120% higher in comparison with commercial flights. In addition, according to the National Transportation and Safety Board (NTSB) Review of Civil Aviation Accidents from 2010[18] and the NTSB 2015/2016 Most Wanted Transportation Safety Improvements factsheets,[19,20] fixed-wing general aviation (GA) accidents accounted for 89% of all accidents and 86% of total fatalities of U.S. civil aviation, where loss of control accounted for approximately 40% of these fatal accidents. The large proportion of fixed-wing GA aircraft accidents related to loss of control means that a concerted research effort towards GA aircraft stall/post-stall flight simulation modeling is required. A comprehensive effort similar to the NASA AvSSP program has not yet been pursued. The "Partnership to Enhance General Aviation Safety, Accessibility, and Sustainability" (PEGASAS) program, was recently formed with the goal of enhancing general aviation safety, accesibility, and sustainability.[21] However, a review of PEGASAS projects shows that the development of stall/upset modeling for the purposes of flight simulation does not fall under its purview.

The use of simulators has been common practice in the past 30 years for pilot training. Simulators allow for pilot training in real world situations and are achieved by ensuring that the simulators mimic the aircraft and environment as realistically as possible. The critical limitation common in most simulators is the lack of fidelity in regimes outside normal flight. One of these limitations relates to aircraft stall. In flight simulators, stall training for most pilots has been limited to "approach to stall" training, that activates a stall warning system or stick shaker, upon which recovery is initiated. The primary reason for the lack of fidelity is that most flight simulators are based on stability derivatives that are only accurate in the linear range of aerodynamic performance. Stall and post-stall effects are highly nonlinear in nature and subsequently are hard to accurately model in real time. A survey of current off-the-shelf flight simulators shows that Microsoft Flight Simulator X,[22] FlightGear,[23] and Prepare3D[24] all mainly use stability derivatives.

Real-time aerodynamic flight simulation via a physics-based component buildup method using the strip theory approach has more recently been used for flight simulation.[25–30] This method has the ability to account for non-linear effects associated with the stall regime and will be used in this study. To properly simulate an aircraft in stall, both steady and unsteady effects need to be modeled.[31] This paper will describe the approach taken to model the steady-state longitudinal aerodynamic forces of a typical GA aircraft in the propeller-off configuration. The approach is validated against a large dataset of experimental wind tunnel results for a typical single-engine low-wing general aviation design.[32] Results from these validations studies are presented and discussed.

II.   Test Case Geometry and Test Conditions

Validation is performed against static wind tunnel test data for a 1/7-scaled and modified version of a Grumman American AA-1 Yankee (single-engine, low-wing GA model).[32] The wind tunnel tests were performed as part of the NASA Stall/Spin Project carried out in the 1970-80s.[33] The low-wing general aviation (LWGA) aircraft is modeled using OpenVSP[34,35] and exported to SolidWorks based on three-views and dimensional characteristics of the model.[32,36] An isometric view of the wireframe mesh and surfaced model is shown in Fig. 1.

The 1/7-th scale LWGA model has a rectangular wing with a 0.5725 ft chord and 3.5 ft span. The wing has a dihedral of 5 deg and is set at an incidence angle (i_W) of 3.5 deg with no geometric twist. The span of the horizontal tail is 1.07 ft, and it is set at an incidence angle (i_{HT}) of -3 deg. The horizontal tail number referenced in Table 1 relates to the vertical location of the horizontal tail with respect to the aircraft centerline. Horizontal tail #3 is located 0.0917 ft above the aircraft centerline, and its root leading edge is aligned with the root leading edge of the vertical tail.

Wind tunnel tests were conducted at a Mach number of 0.2 at Reynolds numbers of $0.288{\times}10^6$ and $3.45{\times}10^6$. Test datasets include full aircraft and individual component force and moment coefficients for angles of attack from -8 to 90 deg and sideslip angles from -10 to 30 deg. In addition, datasets characterizing aerodynamic effects of the aircraft due to elevator, aileron, and rudder deflections are also available. The datasets from Ref. 32 are for a propeller-off configuration. For the current study, only longitudinal aircraft characteristics (C_L, C_D, and C_{Mcg}) at a Reynolds number of $3.45{\times}10^6$ were modeled. The higher Reynolds number case was chosen as it was a closer representation to the full-scale aircraft. The pitching moment results are presented based on the LWGA aircraft center-of-gravity position of $0.255\bar{c}$. Table 1 lists the various LWGA aircraft configurations that the longitudinal aerodynamic model will be validated against.
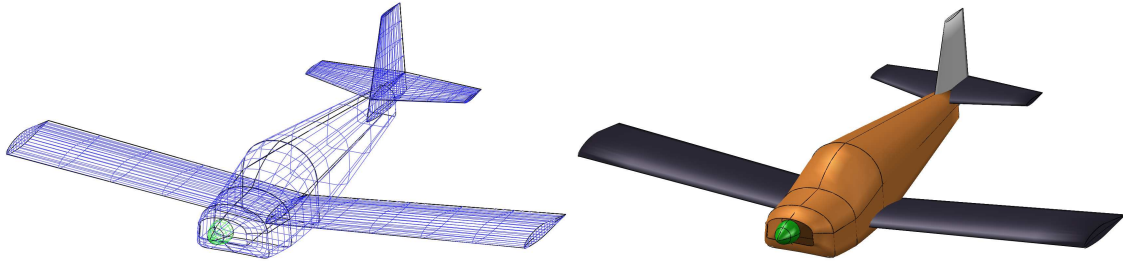

Figure 1. Isometric view of the LWGA model.

Table 1. Low-Wing General Aviation Aircraft Configurations Tested

Configuration	δ_e [deg]	δ_a [deg]	δ_r [deg]
B	0	0	0
BW1	0	0	0
BH3	0	0	0
BV	0	0	0
BW1H3	0	0	0
BW1H3V	0	0	0
BW1H3V	-25	0	0
BW1H3V	15	0	0

B: Fuselage

H3: Horizontal tail #3

W1: Modified NACA 64_2 - 415 airfoil

V: Vertical Tail

American Institute of Aeronautics and Astronautics

III.   Modeling Methodology

The goal of modeling a single-engine GA for stall/upset events is a challenging endeavor given the number of effects that need to be accurately modeled throughout the entire flight envelope. A variety of modeling methods have been used (i.e., stability derivative methods, full aerodynamic lookup tables, etc.). The most robust method, albeit with lower fidelity, that has been employed is a physics-based component-buildup method using the strip theory approach.

In the component-buildup approach, an airplane is separated into its main individual components: propeller, wing, fuselage, horizontal tail, and vertical tail. Each component (apart from the propeller) is then modeled using a strip-theory approach in which individual components are further subdivided into sections. Each of these sections are then subjected to varying local relative flow that is based on aircraft speed, induced flow, kinematics, wind, propeller slipstream, and other interference effects. For the current study, only aircraft speed and induced flow due to shed vortices is considered. Data tables for each of the component sections are derived from wind tunnel results, computational fluid dynamics (CFD) runs, numerical panel methods, and/or semi-empirical methods.The methodology involved in development of each of these data tables will be further discussed in the following subsections.

An integrated non-linear lifting-line theory [25,26,37,38] approach is then used to determine the local induced angle of attack at each strip of the wing and horizontal tail. This method has the ability to account for the effect of individual surface deflection angles and most importantly non-linear effects associated with the stall regime. Components and effects that will contribute to the lateral characteristics of the aircraft (i.e., vertical tail and wake shielding) are not included as only longitudinal aircraft characteristics are modeled in this study.

A.   Airfoil Model

The proper modeling of the aerodynamic performance of airfoils for the wing and horizontal tail is the primary factor that determines the static-stall characteristics of an aircraft. The magnitude of airfoil $C_{l_{max}}$ directly relates to the aircraft flight speed and angle of attack. Consequently, $C_{l_{max}}$ determines the takeoff, approach, and landing characteristics of an aircraft. Thus, for increased simulation fidelity, it is crucial that the stall characteristics of an airfoil ($C_{l_{max}}$, α_{stall}, type of stall, etc.) is accurately predicted.

Broadly, there are four approaches to predicting steady-state airfoil performance: wind tunnel testing, computational fluid dynamics (CFD) simulations, numerical panel methods (e.g., XFOIL [39]), empirical, and semi-empirical methods that use some combination of the previous four methods. Wind tunnel tests are the current main source of accurate airfoil performance data. Airfoil performance data in the pre-stall regime up to stall are widely available both at low [40–45] ($Re \le 500{,}000$) and high [46] ($Re > 500{,}000$) Reynolds numbers. In the post-stall regime, however, only a sparse amount of wind tunnel test data is available. [47–50] In its current state-of-the-art, CFD is used as an ideal tool for design and optimization studies. In addition, it is used to better understand flow behavior around objects. CFD methods, however, still suffer due to the inability to deal with highly separated flows that are typical for a wing in the post-stall regime. [51] In addition, building an accurate set of lookup tables for flight simulation would take prohibitively long even using Reynolds-Averaged Navier Stokes (RANS) CFD simulations. For this study, the authors did not use CFD in the aerodynamic modeling. Instead, numerical panel method codes (with boundary layer integration) such as XFOIL are fast and accurate pre-stall. However, XFOIL is known to overpredict $C_{l_{max}}$ and underpredict minimum drag. [52] The best approach to modeling airfoil performance both pre-stall and post-stall is some combination of the previous three methods together with validated empirical models (i.e., AERODAS model [53]).

The LWGA wing has a rectangular planform and uses a 'modified' NACA 64_2-415 airfoil section. [36] Its horizontal and vertical tail both use the NACA 65_1-012 airfoil sections. A coplot of the original NACA 64_2-415 airfoil against the 'modified' airfoil section is shown in Fig. 2. The difference between the original and modified NACA 64_2-415 airfoils is the amount of aft camber and trailing edge thickness.

To the authors' knowledge, there are no available wind tunnel data sets for the modified NACA 64_2-415 airfoil. Wind tunnel data is, however, available for the original NACA 64_2-415 airfoil. [46] XFOIL and experimental results for the NACA 64_2-415 at $Re = 3 \times 10^6$ are co-plotted in Fig. 3. In addition, given that the LWGA test Reynolds number is 3.45×10^6, XFOIL results for the modified and original NACA 64_2-415
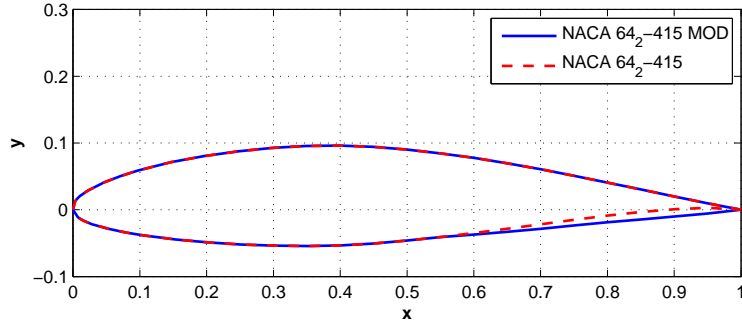
Figure 2. Comparison of original and modified NACA 64$_2$-415 airfoils.
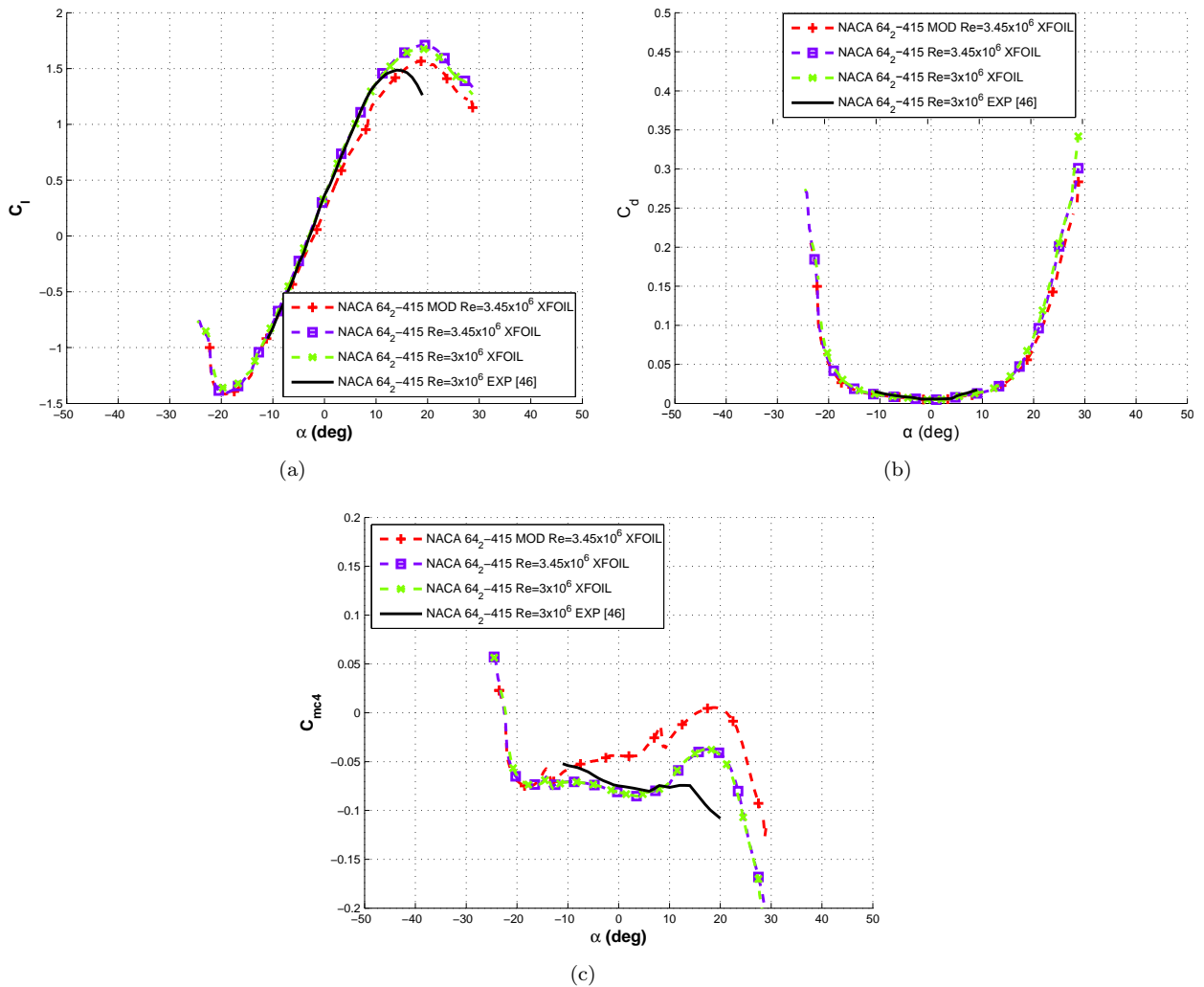

(a)

(b)

(c)

Figure 3. XFOIL and experimental aerodynamic data for NACA 64$_2$-415 modified and baseline airfoil (a) lift curve, (b) drag polars, and (c) moment curves.

airfoil at $Re = 3.45 \times 10^6$ are coplotted. Comparing the XFOIL results for the two airfoils at $Re = 3.45 \times 10^6$, it is evident that the reduction in aft camber in the modified airfoil reduces its $C_{l_{max}}$ and pitch down
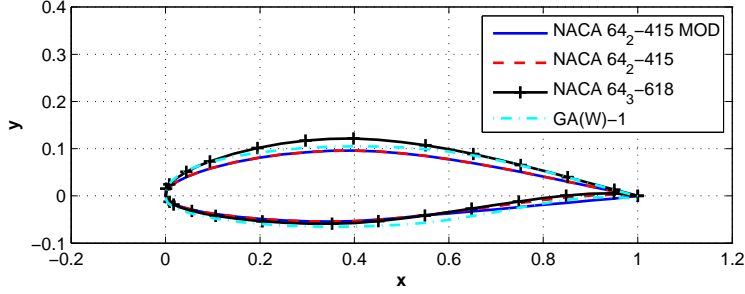
American Institute of Aeronautics and Astronautics

Figure 4. Comparison of original and modified NACA 64₂-415 airfoils, and the NACA 64₃-618 and GA(W)-1 airfoils.

moment. Apart from that, a substantial difference in the $C_{l_{max}}$ and stall angle of attack between the XFOIL and experimental results ($\sim$0.25 and $\sim$7 deg respectively) for the NACA 64$_2$-415 at $Re = 3 \times 10^6$ is observed. The magnitude of the moments also differs between XFOIL and experimental results.

Given the lack of wind tunnel data available for the modified airfoil, experimental results for the NACA 65$_2$-415 airfoil was used. The experimental data for the NACA 65$_2$-415 airfoil provides a conservative estimate of the $C_{l_{max}}$ of the airfoil and as a result would be appropriate in a simulation environment. The XFOIL results in Fig. 3 suggests that the modified NACA 65$_2$-415 airfoil at $Re = 3.45 \times 10^6$ will either have the same or a slightly lower $C_{l_{max}}$ compared with the NACA 65$_2$-415 airfoil. The semi-empirical post-stall airfoil aerodynamic model (AERODAS) introduced by Spera[53] is used for modeling the lift and drag. The AERODAS model is a set of algebraic equations that best fit to 28 stall/post-stall experimental data sets. As opposed to Lindenburg[54] and Tangler and Ostowari,[55] thickness effects are also accounted for in the lift and drag calculations. Given that no experimental data exists post-stall for the airfoil, the drop in lift modeled post-stall may not be accurate. For pitching moment, an empirical post-stall model developed by Montgomerie will be used[56].

Experimental results together with the AERODAS model data for the NACA 64$_2$-415 airfoil from -45 to 90 deg angles of attack are plotted in Fig. 5. In addition, two other cambered airfoils (NACA 64$_3$-618 and GA(W)-1) with available post-stall experimental data and similar geometric parameters (see Fig. 4) are also coplotted in Fig. 5. The geometric characteristics of the airfoils are listed in Table 2.

Table 2. Airfoil Geometric Characteristics

Airfoil	$(t/c)_{max}$	x/c loc. $(t/c)_{max}$	max camber	x/c loc. max. camber	TE angle (deg)	LE Radius (r/c)
NACA 642-415 MOD	0.1497	0.352	0.0207	0.550	18.74	0.01544
NACA 642-415	0.1497	0.352	0.0207	0.550	4.51	0.01544
NACA 643-618	0.1798	0.354	0.0303	0.550	5.13	0.02191
GA(W)-1	0.1698	0.399	0.0241	0.674	3.15	0.03455

B.   Flap Model

The LWGA control surfaces are the flaps, ailerons, elevator, and rudder. Wind tunnel test datasets are only available for aileron, elevator, and rudder deflections. The movement of these control surfaces creates a aerodynamic flap effect that needs to be modeled at the airfoil level. The aerodynamic effects of flap deflections are modeled empirically using methods developed in Torenbeek[57] and McCormick.[58] As a result, increments in the lift, drag, and moments can be quantified based on the flap chord ratio (c_f/c), flap deflection angle (δ_f), and the type of flap (i.e., plain, slotted, etc.) used. Plain flaps are assumed to be used for the 1/7-scaled LWGA model.

American Institute of Aeronautics and Astronautics
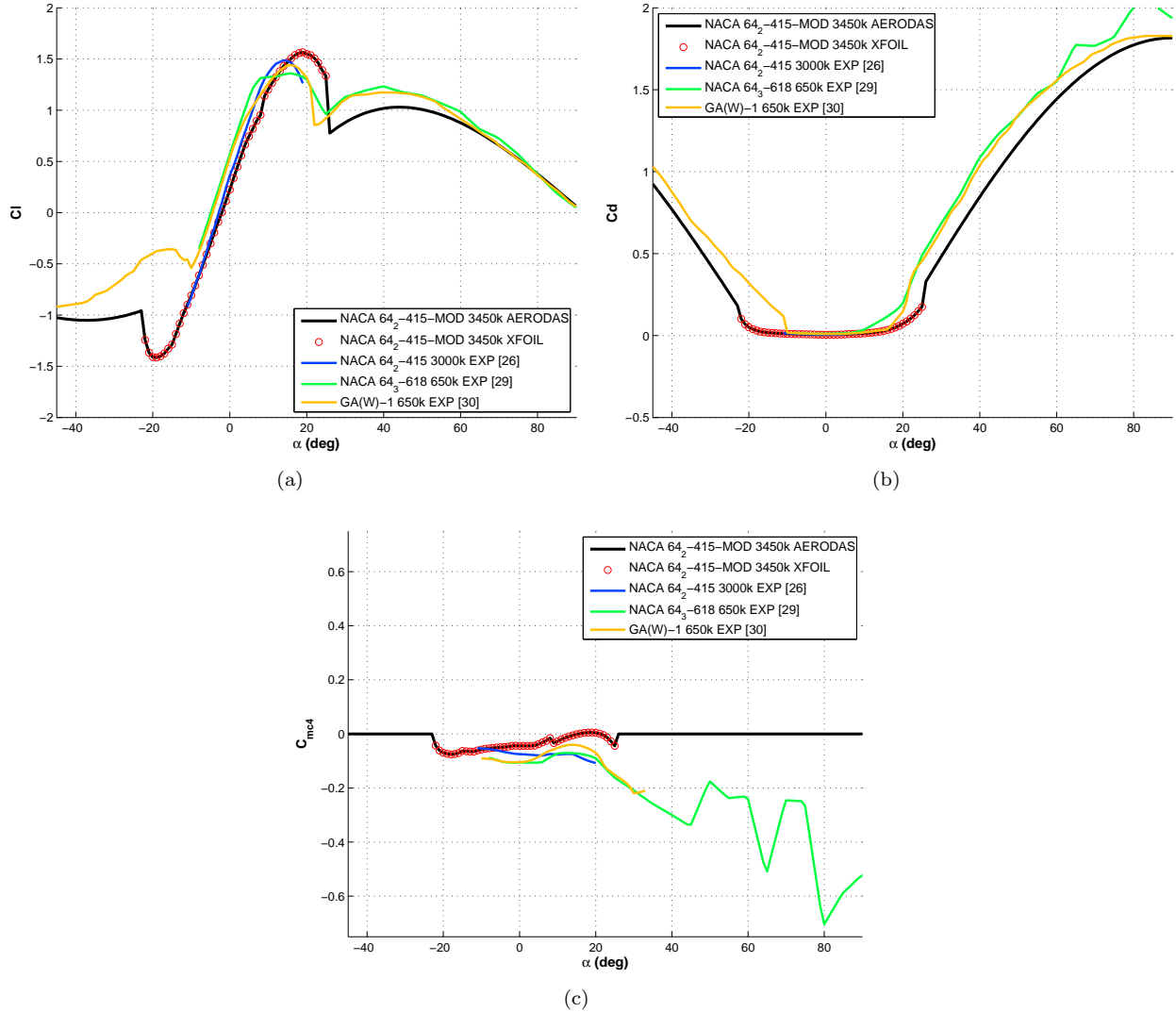
(a)

(b)

(c)

Figure 5. XFOIL and extended airfoil data for the modified NACA 64$_2$-415 airfoil coplotted with experimental data from similarly cambered airfoils with post-stall data: (a) lift, (b) drag, and (c) moment curves.

The increment in airfoil lift due to flap deflection, ΔC_l, is related to the flap effectiveness factor (τ), flap effectiveness correction factor (η), and flap deflection angle, viz,

$$\Delta C_l = C_{l\alpha}\tau\eta\delta_f \tag{1}$$

where the τ is directly related to the flap chord ratio through the relation

$$\tau = 1 - \frac{(\theta_f - \sin\theta_f)}{\pi} \tag{2}$$

$$\theta_f = \cos^{-1}(2\frac{c_f}{c} - 1) \tag{3}$$

As discussed in Ref. 58, an airfoil with a deflected flap stalls at a lower lift coefficient than if the ΔC_l were added to the $C_{l_{max}}$ directly. This fact was accounted for in the flap modeling, where,

$$\Delta C_{l_{max}} = \Delta C_l \ f(\frac{c_f}{c}) \tag{4}$$

The increment of lifting surface drag, ΔC_D, due to flap deflection is related to the flap chord ratio, flap area to surface area ratio ($\frac{S_f}{S}$), and flap deflection angle is given by the relation

$$\Delta C_D = 1.7(c_f/c)^{1.38}(S_f/S)\sin^2\delta_f \tag{5}$$

The moment increment, $\Delta C_{m,c/4}$, is related to the ΔC_l based on thin airfoil theory. Similar to an airfoil with camber, the airfoil is treated as a flat plate with a flap deflected yielding

$$\Delta C_{m,c/4} = -\Delta C_l \frac{2\sin\theta_f - \sin 2\theta_f}{8(\pi - \theta_f + \sin\theta_f)} \tag{6}$$

Only one experimental dataset was found measuring flap effects in the post-stall regime. Wind tunnel tests were performed on a 24% thick airfoil, the NACA 23024, from -180 to 180 deg at a Reynolds number of 0.65×10^6.[49] The flap was located at the 80% chord ($c_f/c = 0.2$) with deflection angles from -60 to 60 deg. Comparisons performed assessing the thickness effects of the airfoil show that post-stall, the NACA 23024 performed aerodynamically similar to a 10% thick airfoil except at the maximum drag (at 90 deg) condition.
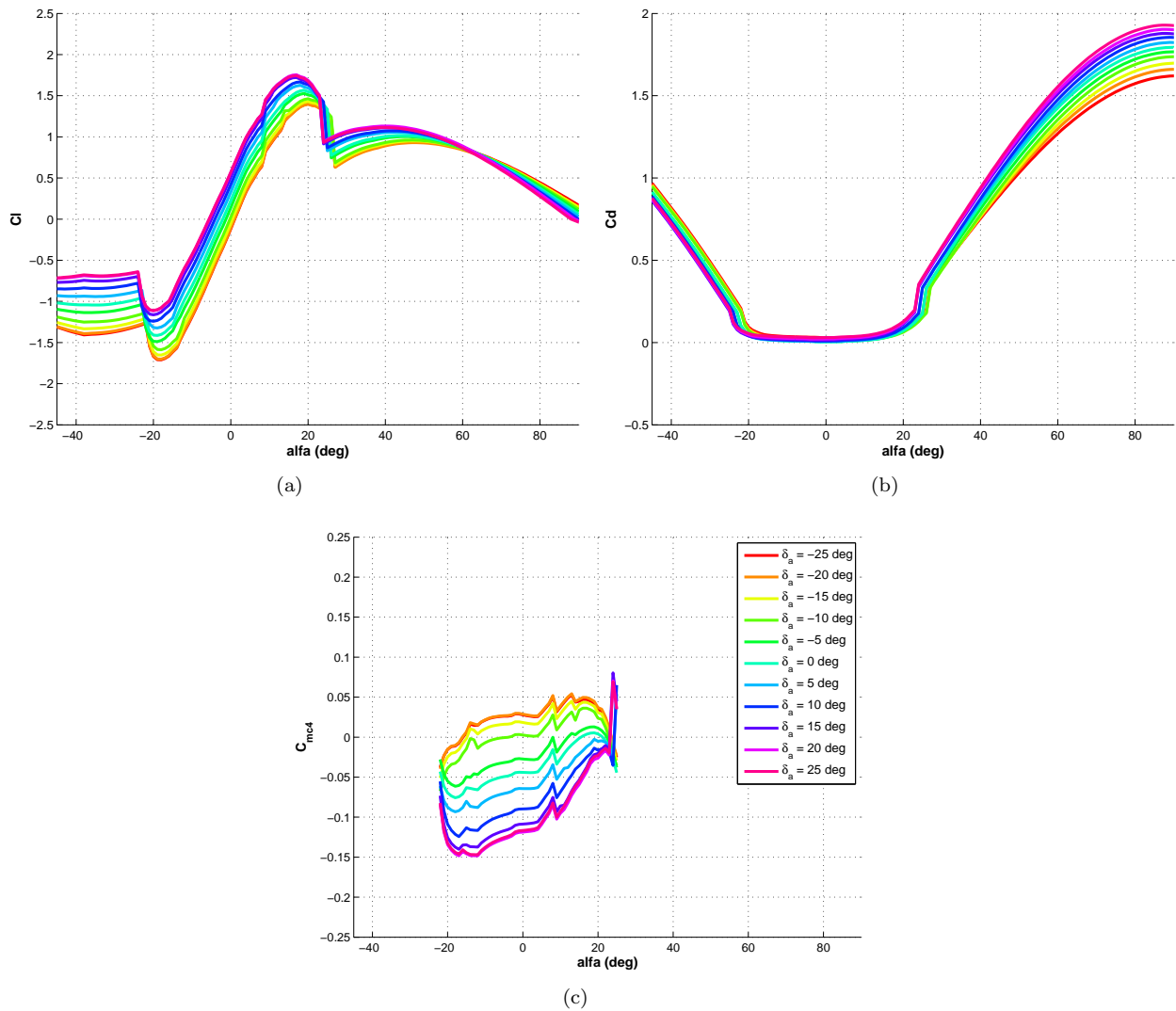
Figure 6. Modeled NACA 64$_2$-415 modified airfoil at $Re = 3.45\times10^6$ for δ_f from -25 to 25 deg (a) lift, (b) drag, and (c) moment.

American Institute of Aeronautics and Astronautics

This means that observations can be taken with sufficient confidence and applied to thinner airfoils. The main observations from the wind tunnel results are the flap effects close to 90 deg. Given that with varying flap deflection, the effective chordline of the airfoil changes, this means that the location of zero lift varies with flap deflection. In addition, the drag coefficient directly relates to the direction of flap deflection. Lift, drag, and pitching moment curves for the wing airfoil for δ_f from -25 to 25 deg are plotted in Fig. 6. As a sanity check for the post-stall drag results, it can be imagined that with a positive flap angle (trailing edge down) at high angles of attack, the airfoil would act like a scoop thereby causing an increase in maximum drag as observed in Fig. 6.

C. Lifting Surface Model (Wing / Horizontal Tail)

An integrated non-linear lifting-line model is used for real-time calculation of the wing and horizontal tail aerodynamics from the airfoil data as required for flight simulation. The method uses lookup tables generated for the airfoil at different angles of attack and flap angles and has been used in research [37,38,59,60] and commercially [28,30] for real-time flight simulation. In the current approach, the influence of the various lifting surfaces on each other are considered. Note that external flow effects (i.e. slipstream effects and wake shielding) are not modeled. The non-linear lifting line calculation methodology is detailed as follows.

1. A planform sketch of the LWGA is shown in Fig. 7. The wing and horizontal tail surfaces are split into n_P spanwise panels (numbered in circles). A bound vortex (black lines) is located at the quarter-chord of these lifting surface panels and lifting-lines (green lines) representing shed vortices that trail from the ends of each panel station (numbered in squares). Each of these lifting-lines trail from a spanwise panel station. In the following equations, the panels are numbered j and the panel stations are numbered k. An iterative process is used to determine lift distribution of the wing at a specific angle of attack.

2. Firstly, the lifting-line method is applied to the wing. The circulation is calculated at each panel station (x_{PS}, y_{PS}, z_{PS}) on the wing. The circulation distribution is initialized as an elliptical distribution such that

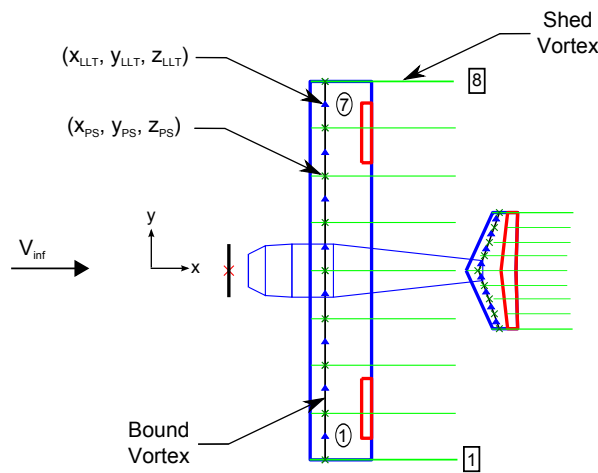$$\Gamma_{init} = \Gamma_0 \sqrt{1 - \left(\frac{2y}{b}\right)^2} \tag{7}$$

Figure 7. Sketch of LWGA lifting-line system.

American Institute of Aeronautics and Astronautics

where the circulation at the center span, Γ_0, is calculated from Kutta-Joukowski Theorem given by

$$\Gamma_0 = \frac{1}{2}V_\infty c_{root} C_l \tag{8}$$

The sectional C_l is based on the effective angle of attack (α_{eff}) and δ_f at each station where

$$\alpha_{eff} = \alpha_{geo} - \alpha_{ind} + i_{surface} \tag{9}$$

The induced angle of attack, α_{ind}, is set to 0 for the first iteration.

3. The circulation is then calculated at each lifting-line point ($x_{LLT}, y_{LLT}, z_{LLT}$). The lifting-line points (blue triangles) are located on the bound vortex at the center of each lifting surface panel. The circulation at each lifting line point is given by

$$\Gamma_{LLT_j} = \frac{\Gamma_{init_j} + \Gamma_{init_{j+1}}}{2} \tag{10}$$

4. The vorticity shed at each spanwise panel station is then calculated using

$$\Gamma_{SV_1} = \Gamma_{LLT_1} \tag{11}$$

$$\Gamma_{SV_{n_P}} = \Gamma_{LLT_{n_P}} \tag{12}$$

$$\Gamma_{SV_j} = \Gamma_{LLT_j} - \Gamma_{LLT_{j-1}} \tag{13}$$

5. Next, the induced velocity at each lifting-line point is calculated due to each trailing vortex. This is done via an extension of the Biot-Savart law.[61] The velocity induced by a shed vortex located at spanwise panel station, k, on the lifting-line point, j, is given by

$$w_{ind_{jk}} = \frac{\Gamma_{SV_k}}{4\pi} \left(\frac{y_{PS_k} - y_{LLT_j}}{(z_{LLT_j} - z_{PS_k})^2 + (y_{LLT_j} - y_{PS_k})^2} \right)$$
$$\left[1.0 + \frac{x_{LLT_j} - x_{PS_k}}{\sqrt{(x_{LLT_j} - x_{PS_k})^2 + (y_{LLT_j} - y_{PS_k})^2 + (z_{LLT_j} - z_{PS_k})^2}} \right] \tag{14}$$

The total velocity induced at each lifting-line point, j, due to the shed vortices is then summed, viz

$$w_{ind_j} = \sum_{k=1}^{n_P+1} w_{ind_{jk}} \tag{15}$$

6. Once the induced velocity at each lifting-line point is calculated, the new induced angle of attack relative to the airfoil chordline at each lifting-line point is calculated as

$$\alpha_{ind_j} = \tan^{-1} \left(\frac{-w_{ind_j}}{V_\infty} \right) \tag{16}$$

7. The sectional lift coefficient C_l is interpolated from airfoil lookup tables based on the new α_{eff_j} (calculated using Eq. 9) and δ_{f_j} at each lifting-line point.

8. The induced velocity due to the shed vortices requires for the calculation of a new relative velocity at each lifting line point, that is

$$V_{rel_j} = \sqrt{V_\infty^2 + w_{ind_j}^2} \tag{17}$$

9. The direction of the relative velocity causes a normal force that has a lift and induced drag component given by

$$N'_j = \frac{L'_j}{\cos(\alpha_{ind_j})} \tag{18}$$

and

$$N'_j = \rho V_{rel_j} \Gamma_{LLT_j} \tag{19}$$

resulting in the calculation of the new circulation distribution at the lifting-line point that is

$$\Gamma_{LLT,new_j} = \frac{1}{2} \frac{V_\infty^2}{V_{rel_j}} \frac{1}{\cos(\alpha_{ind_j}) c_j C_{l_j}} \tag{20}$$

The chord is based on the chordwise distribution over the wing. For the LWGA wing, the chordwise distribution is constant.

10. The circulation distribution to be used for the next iteration is a combination of the previous circulation together with the newly calculated circulation distribution. Anderson[38] suggests the following equation, where D is the damping factor for the iterations

$$\Gamma_{LLT_j} = D\Gamma_{LLT,new_j} + (1-D)\Gamma_{LLT_j} \tag{21}$$

A damping factor D of 0.05 to 0.1 is used.

11. Steps 4–10 are repeated until a criteria for convergence is satified. The convergence criteria is given by

$$\frac{\sum_{j=1}^{n_P}(\Gamma_{LLT,new_j} - \Gamma_{LLT_j})^2}{n_P} \leq 0.00001 \tag{22}$$

12. Once convergence is satisfied, the total lift for the wing is determined by summing the lift contributions of the individual panels of the wing. Induced drag is also similarly calculated using

$$L = \sum_{j=1}^{n_P} \rho V_{rel_j} \Gamma_{LLT_j} \cos(\alpha_{ind_j}) \Delta y_{panel_j} \tag{23}$$

$$D_{ind} = \sum_{j=1}^{n_P} \rho V_{rel_j} \Gamma_{LLT_j} \sin(\alpha_{ind_j}) \Delta y_{panel_j} \tag{24}$$

The profile drag and pitching moment of the lifting surface are calculated by summing the individual section contributions. This method ensures that control surface deflections and other effects local to a specifc panel section are included in the overall calculation. The total drag for the lifting surface is calculated by summing the profile drag and induced drag contributions. For the current study, each lifting surface is split into 30 panel sections and requires 100-200 iterations to converge.
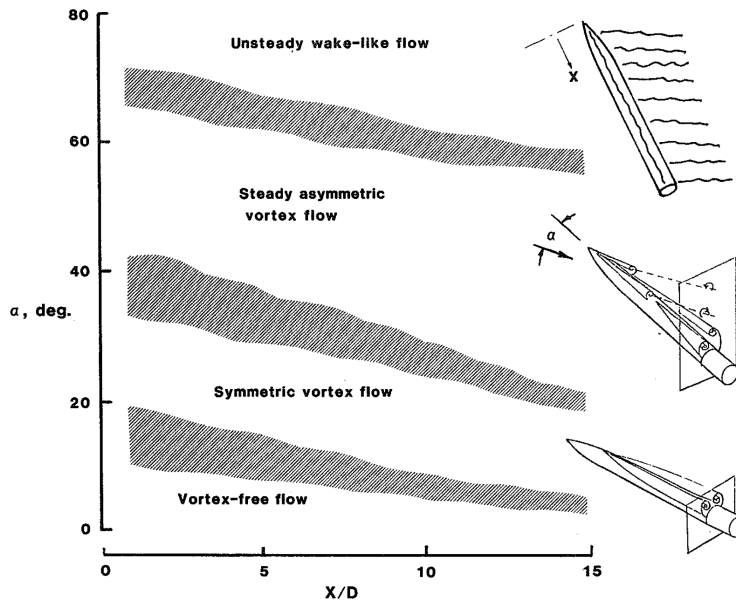
American Institute of Aeronautics and Astronautics

Figure 8. Correlation of fuselage fineness ratio, x/D, angle of attack and type of wake generated[63].

D.   Fuselage Modeling

The fuselage is a complex body to aerodynamically characterize. Figure 8 shows the flow over a fuselage-type body at varying angles of attack. Vortex-free flow exists at low angles of attack. The aerodynamic forces in this angle of attack range can be predicted by slender-body potential flow theory. The normal force therefore increases linearly with angle of attack[62]. At higher angles of attack, the flow starts to separate from the fuselage body. Vortex flows dominate in this high angle of attack range causing the normal force to increase nonlinearly. Initially, the vortex sheets that form due to flow separation are symmetric in nature. As the angle of attack increases, the vortex sheets become asymmetrical thereby generating large "out-of-plane" forces and mitigating the normal force rise. At high angles of attack, the flow transitions to more unsteady wake-like flow structure similar to cylinders normal to the flow.

It can therefore be deduced that the issue of proper modeling of the fuselage lies with its varying cross-section area and shape. The varying cross-section of the fuselage combined with the local angle of attack, sideslip angle, and flight Reynolds number means that there are a lot of variables at play. Given that these bodies are mostly blunt, any angle of attack larger than zero creates an appreciable amount of viscous separated flow at different parts of the fuselage. A critical issue in dealing with viscous effects lies with the different cross-section shapes of the fuselage and its associated Reynolds number. Similar to the flow around a cylinder, the flow around the fuselage may be supercritical or subcritical in nature. The change in flow behavior with angle of attack (subcritical to supercritical) may cause a change in the direction of the side forces on the fuselage thereby affecting its lateral stability. The main forces generated by an aircraft fuselage are normal (C_{N_F}), axial (C_{A_F}), and side (C_{Y_F}) forces. Pitching (C_{m_F}) and yawing moments ($C_{N_{yaw_F}}$) are also generated by the fuselage. The axial and normal forces can be decomposed to give the lift (C_{L_F}) and drag (C_{D_F}) of the fuselage using

$$C_{L_F} = C_{N_F} \cos \alpha_{geo} - C_{A_F} \sin \alpha_{geo} \tag{25}$$

$$C_{D_F} = C_{N_F} \sin \alpha_{geo} - C_{A_F} \cos \alpha_{geo} \tag{26}$$

In order to better understand the magnitudes and directions of the forces on a typical fuselage some results from Jorgensen and Brownson[64] for tests done on a space-shuttle type body at a Mach number of 0.3

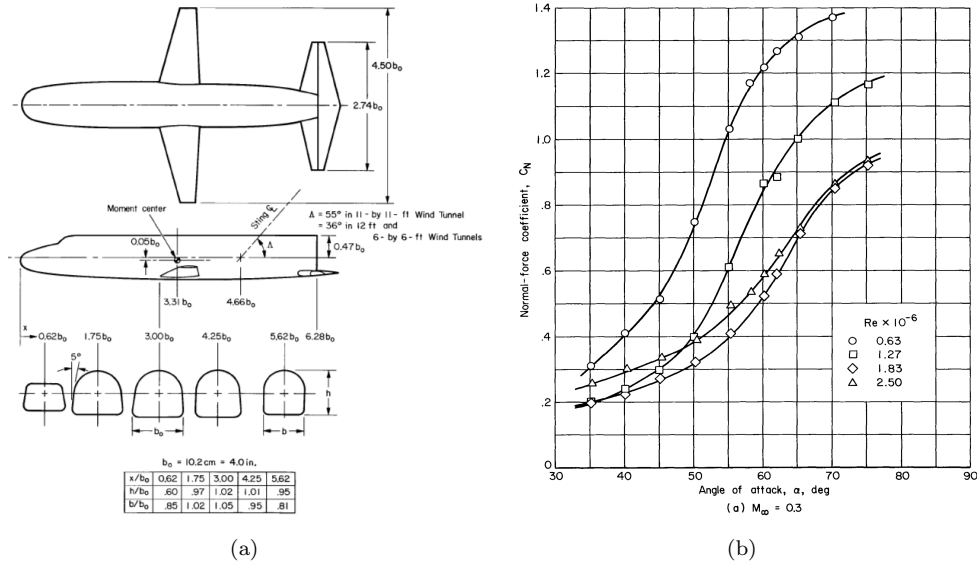American Institute of Aeronautics and Astronautics

Figure 9. (a) Top and side view of body-wing-tail of a space shuttle-type body, and (b) effect of Reynolds number on normal force coefficient with angle of attack for the space shuttle-type body (taken from Ref. ??).
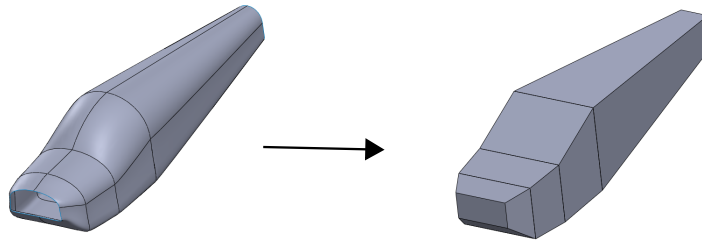

Figure 10. Low-wing GA aircraft actual fuselage and simplified fuselage isometric view.

($\sim$incompressible) are shown in Fig. 9(a). The normal force coefficient curves for different Reynolds numbers for the space-shuttle type body is also shown in Fig. 9(b). As Reynolds number decreases the overall normal force coefficient decreases. Jorgenson and Brownson[64] also demonstrate that there is a significant effect of corner radius on the cross-sectional drag, C_{dn}, of 2-D and 3-D bodies at all Reynolds numbers.

Looking at the LWGA fuselage (Fig. 10), the cross section varies from an oval-like shape to a rectangle with curved/filleted corners. As a simplification, the fuselage is divided into four separate sections with five cross-sections located at different axial stations as shown in Fig. 10. Each section of the fuselage is modeled as a quadrilateral based on the location of its vertices. The model is then used to calculate the centroid, frontal area, planform area, and wetted areas of the fuselage. The wetted areas are used in calculating the surface skin friction coefficient ($C_{A_{SF_F}}$) of the fuselage. As per McCormick,[58] the transition Reynolds number was set to 300,000 (critical Reynolds number for a flat plate), and the total skin friction drag was calculated accordingly. Each of the five sections are then assigned specific shapes for which cross-sectional drag data is available and that closely matches them to the original fuselage (i.e., horizontal rectangle, circle, rounded square, rounded rectangle, etc.).

The methodology used for all normal, axial, and moment force calculations is based on the method developed by Jorgensen[65] derived from Allen and Perkin,[66] and Kelley.[62] The method is an engineering-type procedure that combines the slender-body potential theory and viscous cross-flow terms to calculate

American Institute of Aeronautics and Astronautics

the normal force and pitching moment by way of

$$C_{N_F} = C_{N_{SB_F}} + C_{N_{CF_F}} \tag{27}$$

$$C_{m_F} = C_{m_{SB_F}} + C_{m_{CF_F}} \tag{28}$$

where the slender body (SB) potential theory terms are given by

$$C_{N_{SB_F}} = \left(\frac{A_b}{A_r}\right) \sin(2\alpha) \cos\left(\frac{\alpha}{2}\right) \left(\frac{C_n}{C_{n0}}\right)_{SBave} \cos\beta \tag{29}$$

$$C_{M_{SB_F}} = -\left[\left(\frac{V_F - A_b x_m}{A_r d_{eq}}\right) \sin(2\alpha) \cos\left(\frac{\alpha}{2}\right)\right] \left(\frac{C_n}{C_{n0}}\right)_{SB_{ave}} \cos\beta \tag{30}$$

The term $\left(\frac{C_n}{C_{n0}}\right)_{SB_{ave}}$ is a ratio that varies from 1.19 at $k = 0$ (no corner radius) to 1.00 at $k = 0.5$ (completely circular cross section). The term is also averaged from the four separate sections. The $\cos\beta$ term is included to correct for sideslip effects. The equivalent diameter (d_{eq}) is calculated based on the width (b_0) and corner radius (k) of the square or rectangular cross section using

$$d_{eq} = 2b_0 \sqrt{\frac{1 - (4 - \pi)k^2}{\pi}} \tag{31}$$

where

$$k = \frac{r}{b_0} \tag{32}$$

The crossflow terms for normal force and pitching moment are given by

$$C_{N_{CF_F}} = \frac{N_{CF_F}}{qA_r} = \frac{\eta_F \sin^2(\alpha)}{A_r} \int_0^l b_0 C_{dn} \frac{b_0}{d_{eq}} dx \tag{33}$$

$$C_{m_{CF_F}} = \frac{N_{CF_F}}{qA_r c} = \frac{\eta \sin^2(\alpha)}{A_r d_{eq}} \int_0^l b_0 C_{dn} \frac{b_0}{d_{eq}} (x_m - x_c) dx \tag{34}$$

The cross-flow drag coefficient C_{dn} is a function of both Reynolds number and sideslip angle β. Since most experimental values of C_{dn} are based on cross-sectional width, they must be multiplied by b_0/d_{eq} prior to being used in Eqs. 33 and 34. The C_{dn} results from various shaped cylinders (rounded square, circle, rounder rectangle) at different sideslip angles were taken from Polhamus.[67] Wind tunnel results (downstream force coefficient C_x and side force coefficient C_y) for these various shaped cylinders were taken from 0 to 45 deg sideslip over a Reynolds number range between 100,000 and 2,000,000. The results can be constructed to extend to -180 to $+180$ deg sideslip. Surface plots for the C_x and C_y of a circular cylinder are shown in Fig. 11. From Fig. 11, it is observed that the cylinder has the largest C_x (positive downstream) and zero C_y (positive in the direction of sideslip) at a zero sideslip angle. With a positive sideslip angle, the C_y value increases to a maximum at 90 deg sideslip, and the C_x value decreases to a value of zero at 90 deg sideslip. The crossflow drag proportionality factor η_F is used to correct the 2D drag of the cylinder for three dimensional effects. It is the ratio of the drag coefficient for a finite length cylinder to that for an infinite length cylinder and is an empirical value based on experimental data.
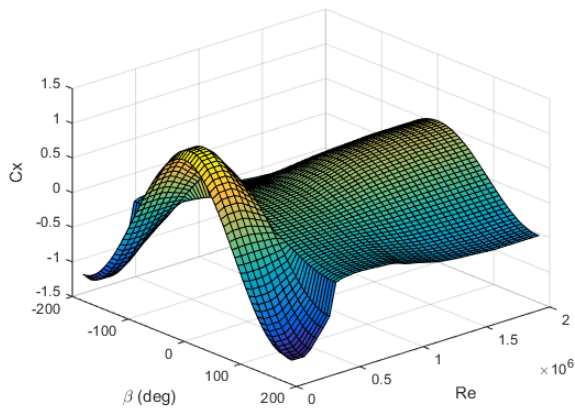
(a)
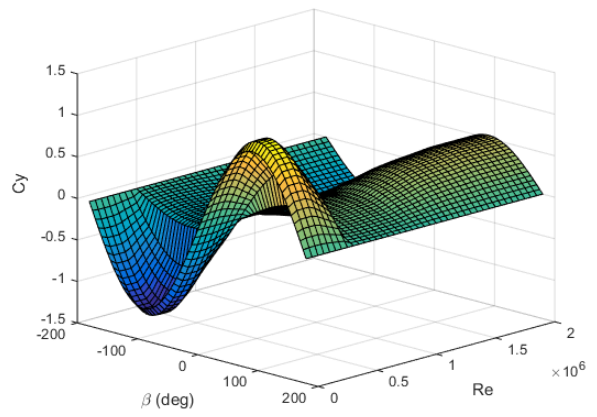
(b)

Figure 11. Forces on a cylinder as a function of Reynolds number and sideslip angle: (a) C_X, (b) C_Y.

IV. Results and Discussion

The methods discussed in Sec. III detail the aerodynamic modeling of the longitudinal characteristics of the aircraft in the propeller-off state. The current section presents results of the developed aerodynamic model for the chosen low-wing General Aviation aircraft. The longitudinal aerodynamics (C_L, C_D, and C_{Mcg}) results of the model will be presented with wind tunnel results at a Reynolds number of 3.45×10^6. All results are non-dimensionalized by the LWGA wing area and results are presented for angles of attack from -10 to 40 deg. Pitching moment results are presented based on the LWGA aircraft center-of-gravity position of $0.255\bar{c}$. The configurations mainly compared are as detailed in Table 1. All lift, drag, and pitching moment coefficient plot limits are maintained the same to facilitate easier comparison between the different sets of results presented.

A. Fuselage Only

As decribed in Section III.D, the fuselage of the LWGA is first divided into four separate sections with quadrilateral cross-sections assigned to a shape with known cross-sectional data. Cross-section data to be used in the fuselage modeling calculations are taken from Ref. 63. Given that only longitudinal characteristics are modeled, the zero sideslip cases are only required and the side force effects are ignored.

The calculated lift, drag and pitching moment coefficients for the fuselage are coplotted together with wind tunnel results from Ref. 32 in Fig. 12. From the results, the calculated lift and drag coefficients of
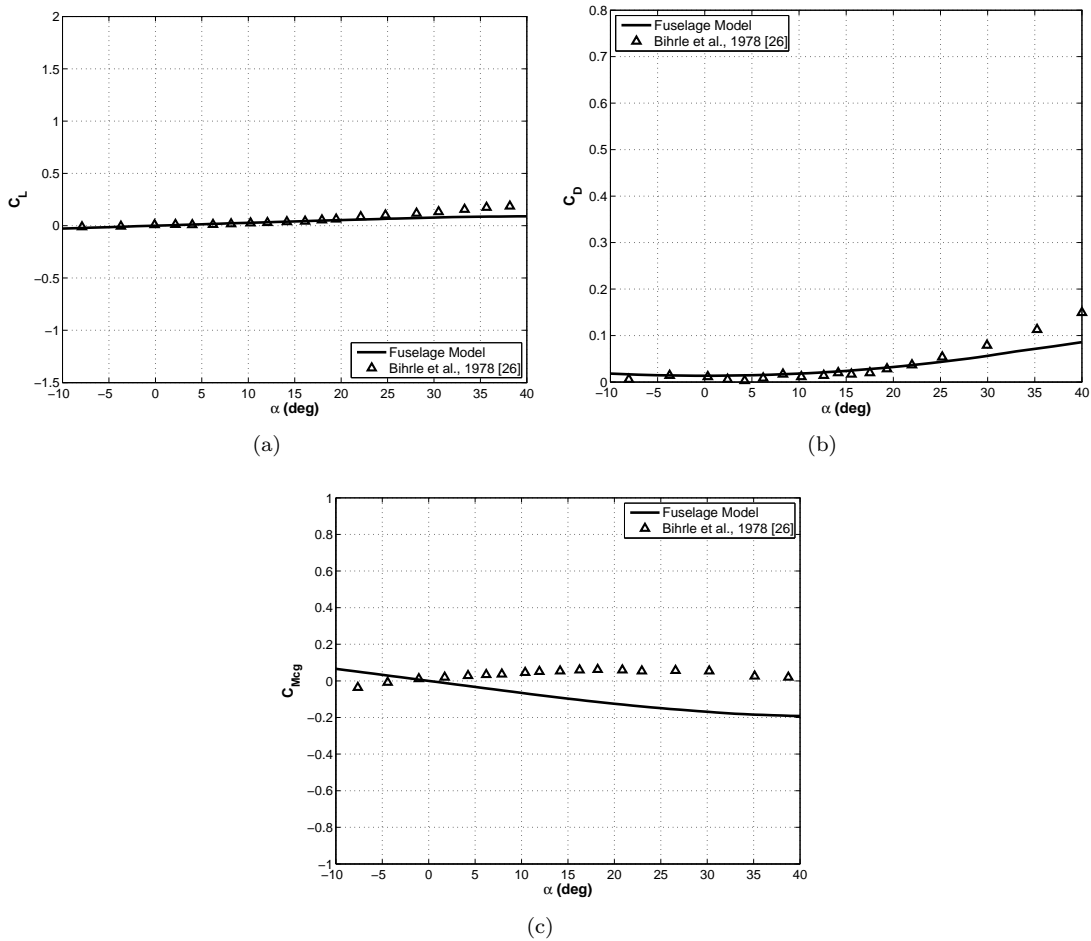

Figure 12. (a) Lift, (b) drag, and (c) pitching moment coefficients of LWGA fuselage at Re of $3.45{\times}10^6$.

American Institute of Aeronautics and Astronautics

the fuselage align well with the wind tunnel results at low angles of attack ($\alpha \leq 20$ deg). The results deviate however, at high angles of attack with the model underpredicting both lift and drag coefficients. The pitching moment results for the fuselage also do not match with the validation data. According to Jorgensen and Brownson,[64] the pitching moment of the fuselage should be increasingly negative (higher pitch-down moment) with increasing angle of attack as long as the center of lift of the fuselage is aft of the center of gravity of the aircraft. The wind tunnel results for the fuselage however indicate that the center of lift of the LWGA fuselage varies with angle of attack.

B.   Fuselage and Wing Only

The next configuration analyzed is the fuselage-wing case. Experimental data for the NACA 64_2-415 airfoil was used for the wing. Non-linear lifting line theory was used in calculating the lift and induced drag of the wing as detailed in Section III.C. The wing was divided into 30 spanwise panels. The converged lift coefficient distribution along the LWGA wing at various angles of attack is shown in Fig. 13. The black line represents the wing when viewed from behind. The effect of the fuselage is modeled as a region of zero lift at the center-span of the wing as shown in Fig. 13. The non-linear lifting line process is iterated until convergence. The red lines indicate the location of the aileron which for this case is not deflected.

The calculated fuselage-wing configuration lift, drag, and pitching moment coefficients are coplotted with wind tunnel data from Ref. 32 in Fig. 14. In addition, individual component results are coplotted to show their contributions to the computed coefficients. The lift and drag coefficients give good agreement with the wind tunnel results. The computed lift coefficients (Fig. 14(a)) show an overprediction in maximum lift and also a larger drop in lift post-stall when compared to the wind tunnel results. One of the primary reasons for the discrepancy is the unavailability of experimental results for the modified NACA 64_2-415 airfoil. Therefore, empirical methods had to be relied upon in modeling the stall and post-stall aerodynamic characteristics of the airfoil. The computed drag coefficients [Fig. 14(b)] matched the wind tunnel results in terms of its minimum drag. The wind tunnel results however show a wider drag bucket and a less precipitious drag rise at high angles of attack compared to the computed drag coefficients. As discussed in the prior section, the pitching moment coefficient [Fig. 14(c)] results differ mainly due to the effect of the fuselage. Given that the center of gravity is located slightly aft of the quarter chord of the wing and that the airfoil has a relatively constant negative pitching moment pre-stall [see Fig. 3(c)] the wing pitching moment contribution (red dashed line) is small to the overall aircraft.

C.   Fuselage and Horizontal Tail Only

Similar to the previous section, for the fuselage-horizontal tail configuration, the horizontal tail was divided into 30 spanwise panels and the forces were computed using non-linear lifting line theory. The lift distribution
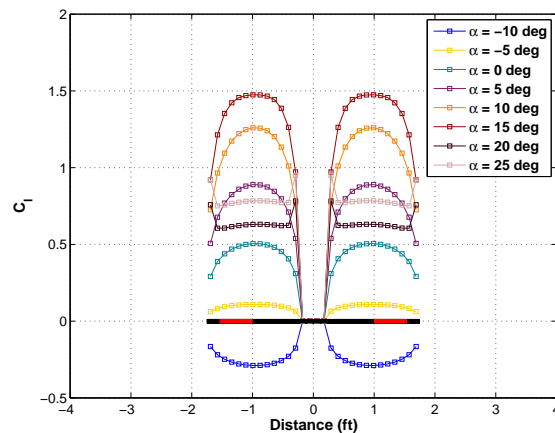

Figure 13. Lift distribution of LWGA wing in the fuselage-wing configuration at a Reynolds number of 3.45×10^6 at 5 deg angle of attack increments.
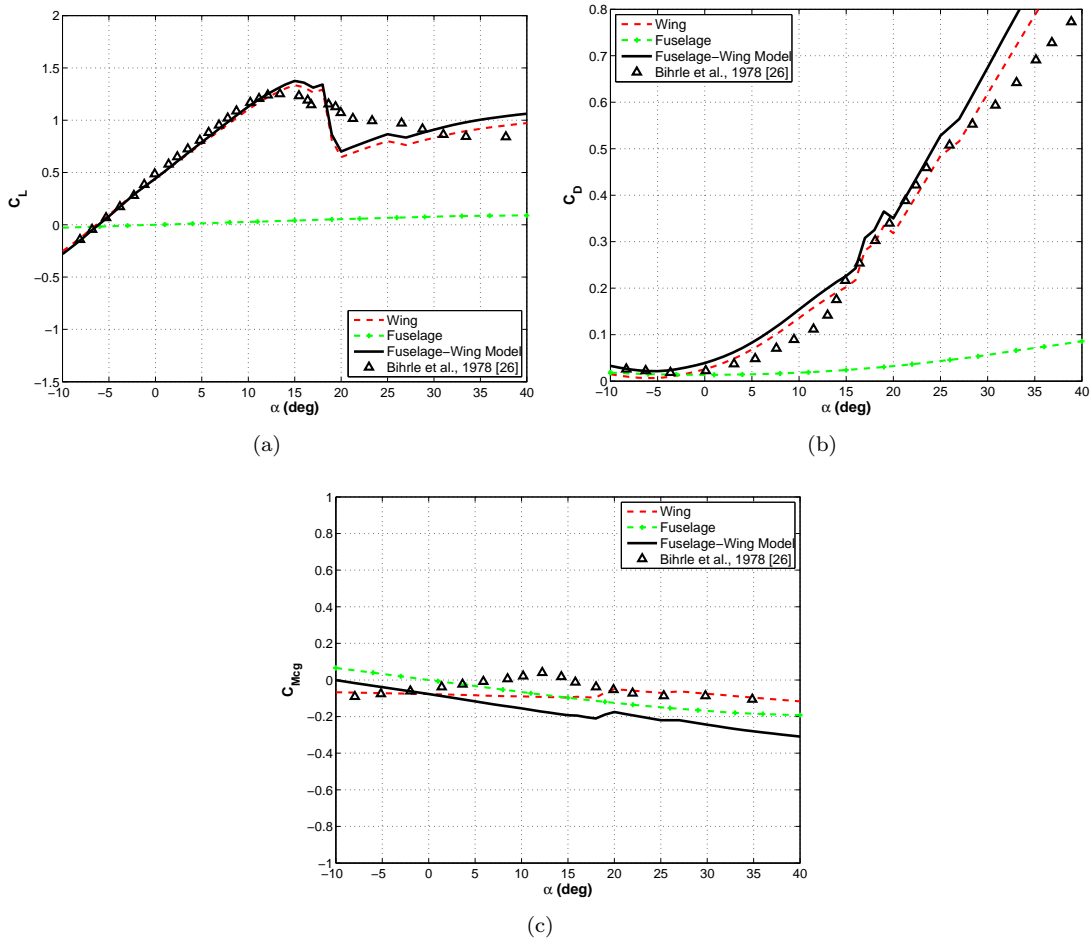
American Institute of Aeronautics and Astronautics

(a)

(b)

(c)

Figure 14. LWGA fuselage-wing configuation (a) lift, (b) drag, and (c) pitching moment coefficients at Re **of** 3.45×10^6**.**

along the LWGA horizontal tail at various angles of attack is shown in Fig. 15. The black line indicates the span of the horizontal tail when viewed from behind. Given that there is no wing for this configuration, only the downwash due to the horizontal tail shed vortices are used to calculated the induced angle of attack at each horizontal tail panel. The change in lift coefficient distribution can be observed with varying geometric angle of attack. A drop in the lift coefficient distribution is observed between 25 and 30 deg angle of attack indicative of stall.

The calculated fuselage-horizontal tail lift, drag, and pitching moment coefficients are coplotted with individual component contributions and wind tunnel data from Ref. 32 in Fig. 16. The lift, drag, and pitching moments all provide good agreement against the wind tunnel results. It has to be noted that the horizontal tail wind tunnel results do not show any clear stall characteristics (loss of lift) in comparison to the computed results. The sharp stall characteristics observed from the computed results are purely as a result of a sharp stall being modeled at the airfoil level. The low aspect ratio and sweep of the LWGA tail could be contributing factors to the mild stall characteristics observed in the wind tunnel results. These effects are difficult to model since non-linear lifting line theory does not account for spanwise-flow effects.

D. Fuselage, Wing, and Horizontal Tail Only

The fourth configuration analyzed is the fuselage-wing-horizontal tail configuration with no control surfaces deflected. In this case, an integrated non-linear lifting line method was required as the effect of the shed vortices of the wing needed to be included in the downwash calculations for the horizontal tail. The lift
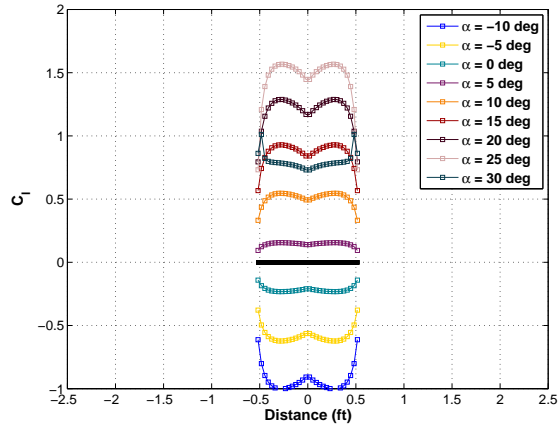
American Institute of Aeronautics and Astronautics

Figure 15. Lift distribution of LWGA horizontal tail for the fuselage-horizontal tail configuration at a Reynolds number of $3.45{\times}10^6$ at 5 deg angle of attack increments.
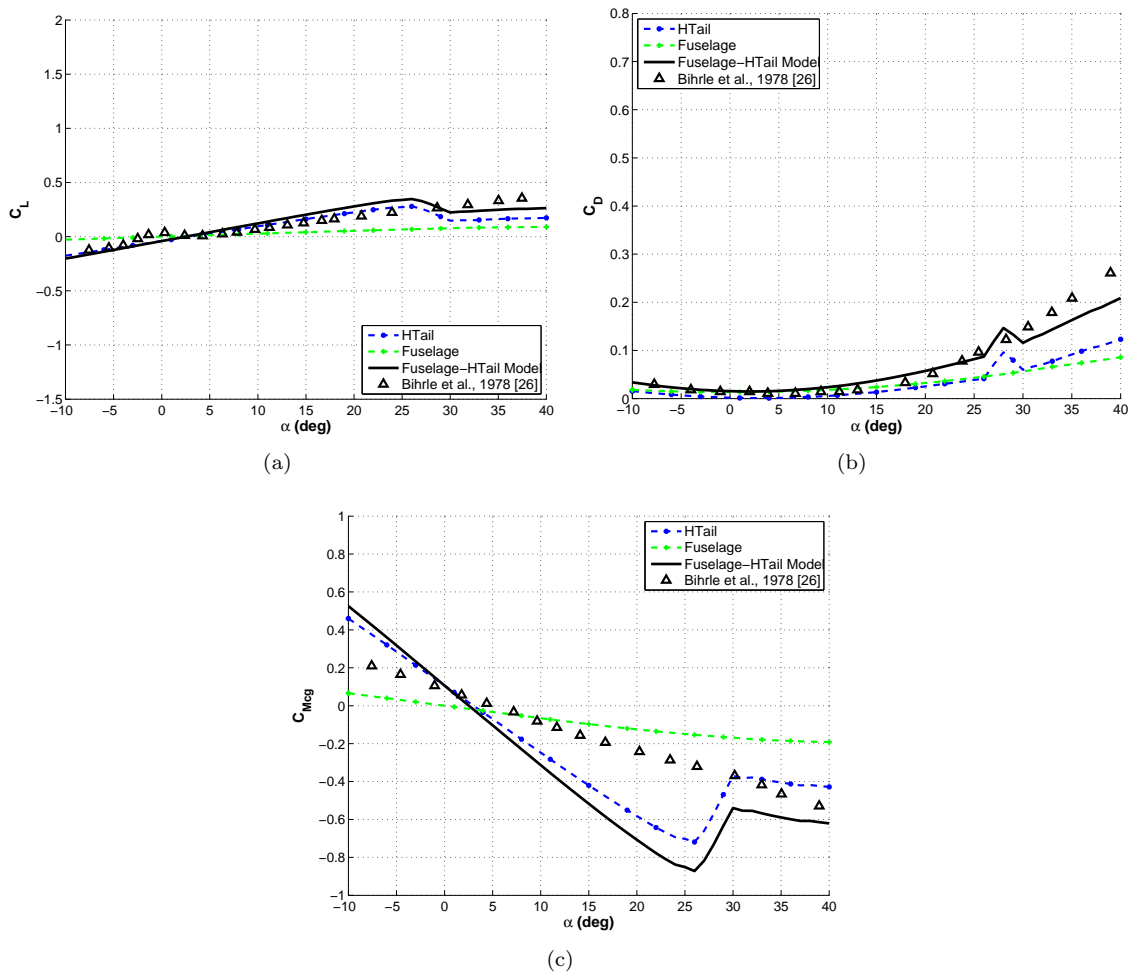

(a)

(b)

(c)

Figure 16. LWGA fuselage-horizontal tail configuration (a) lift, (b) drag, and (c) pitching moment coefficients at Re of $3.45{\times}10^6$.

distribution of the wing was similar to the fuselage-wing configuration as shown in Fig. 13. The resultant lift distribution on the horizontal tail for this configuration is shown in Fig. 17. It is markedly different from the fuselage-horizontal tail configuration (see Fig. 15). When comparing both sets of lift distributions it is clear that the presence of a wing forward of the horizontal tail has a substantial effect on the flow characteristics the horizontal tail experiences. These effects will also be compounded when the control surfaces on the wing are also deflected.

Computed lift, drag, and pitching moment results for the fuselage-wing-horizontal tail configuration are presented in Fig. 18 as the 'Combined Model' configuration. The results are coplotted against wind tunnel results and individual component contributions (wing, horizontal tail, and fuselage). The computed results obtained show excellent agreement for lift and drag and accurate trends are exhibited in the pitching moments. Critically, for the case of lift [Fig. 18(a)], the lift curve slope, zero-lift angle of attack, and the maximum lift point are all accurately captured. The computed results shown a sharp drop in stall that is attributable to the sharp stall modeled at the airfoil level. The minimum drag of the 'Combined Model' case matches with that of the wind tunnel test data [Fig. 18(b)]. In addition, the drag rise with angle of attack also matches well. The slope and magnitude of the moment curve aligns with that of the wind tunnel results [Fig. 18(c)]. The difference observed between the computed and wind tunnel pitching moments could be attributed to the inaccurate fuselage pitching moments noted previously.

E. Fuselage, Wing, Horizontal Tail, and Elevator

The final configuration analzed was the fuselage-wing-horizontal tail with the elevator deflected at -25 and 15 deg (positive trailing edge down). The wing lift distribution was the same as that shown in Fig. 13. However, the horizontal tail lift distribution varies based on the deflection angle of the elevator. Figure 19 shows the lift distribution of the horizontal tail for both elevator deflection angles. From the lift distribution plots, the effect of the elevator deflection is clearly observed where higher lift coefficients are obtained for $\delta_e = 15$ deg case [Fig. 19(b)] compared to the $\delta_e = -25$ deg case [Fig. 19(a)]. Note that the effect of the wing shed vortices are also included in the calculations.

The effects of the elevator deflection on the aerodynamic performance of the aircraft are clearly exhibited in the lift characteristics of the 'Combined Model' curves shown in Fig. 20. Coplotted on the figure are lift results for the wind tunnel case and also individual component contributions. Note that the wind tunnel results are with the vertical tail included. However, since the vertical has negligible contributions to the longitudinal aircraft characteristics at zero sideslip angles, it was deemed an acceptable comparison case. Both 'Combined Model' lift curve slopes, zero-lift angles of attack and maximum lifts closely matched the wind tunnel results exhibiting how accurately the integrated non-linear lifting line method captures critical characteristics of the aircraft up to and past stall. Again as per previous configuration comparisons, in the
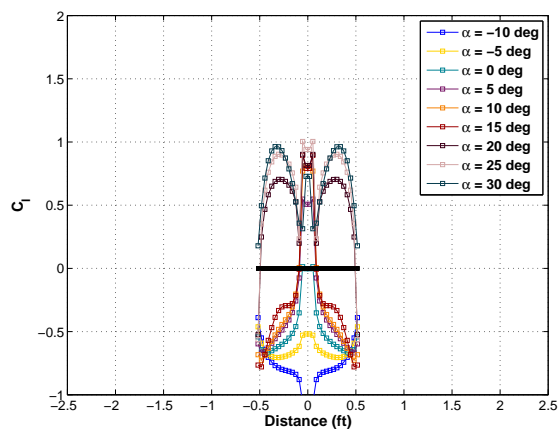

Figure 17. Lift distribution of LWGA horizontal tail for the fuselage-wing-horizontal tail configuration at a Reynolds number of 3.45×10^6 at 5 deg angle of attack increments.
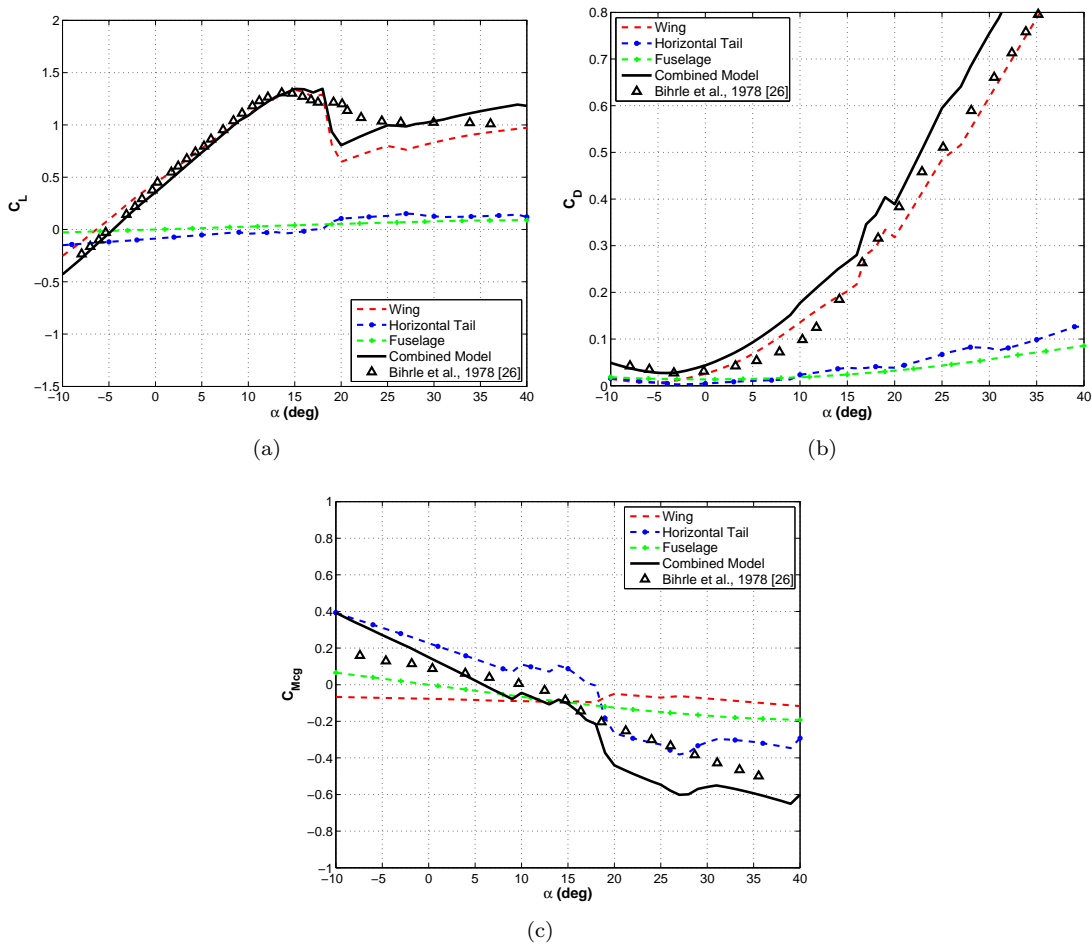
American Institute of Aeronautics and Astronautics

(a)

(b)

(c)

Figure 18. (a) Lift, (b) drag, and (c) pitching moment coefficients of LWGA fuselage-wing-horizontal tail at Re **of** 3.45×10^6**.**
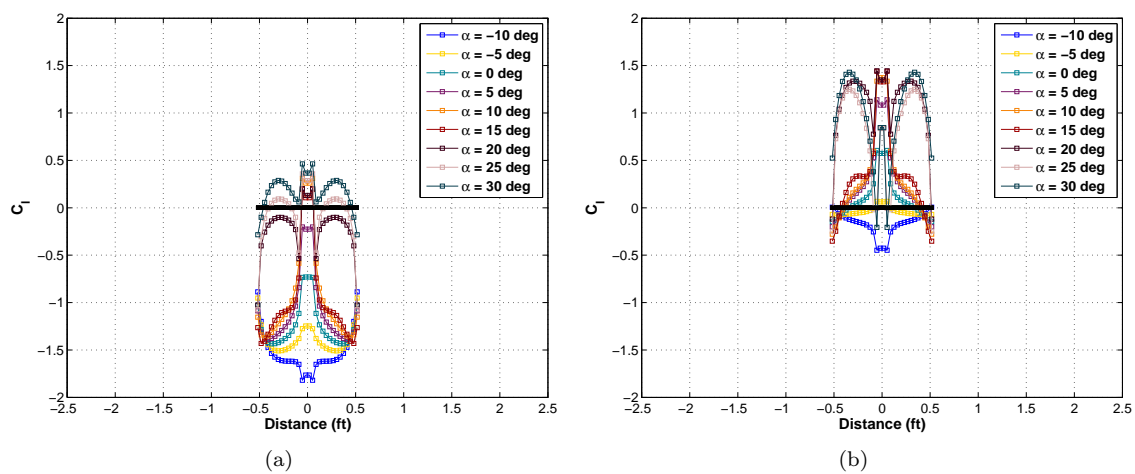

(a)

(b)

Figure 19. Lift distribution of LWGA horizontal tail for the fuselage-wing-horizontal tail configuration at Re **of** 3.45×10^6 **at 5 deg angle of attack increments and (a)** $\delta_e = -25$ **deg, and (b)** $\delta_e = 15$ **deg.**
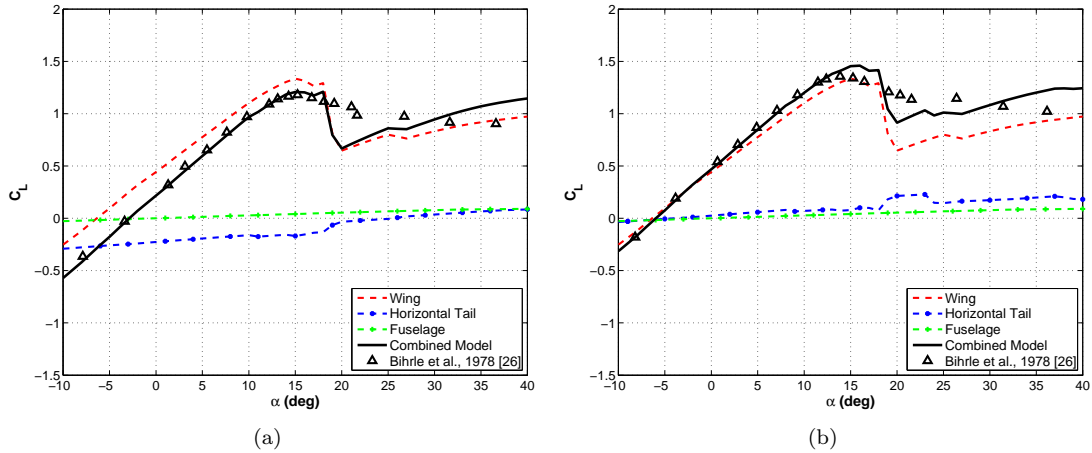
Figure 20. Lift of LWGA fuselage-wing-horizontal tail at Re of 3.45×10^6 and δ_e of (a) -25 deg, (b) 15 deg.
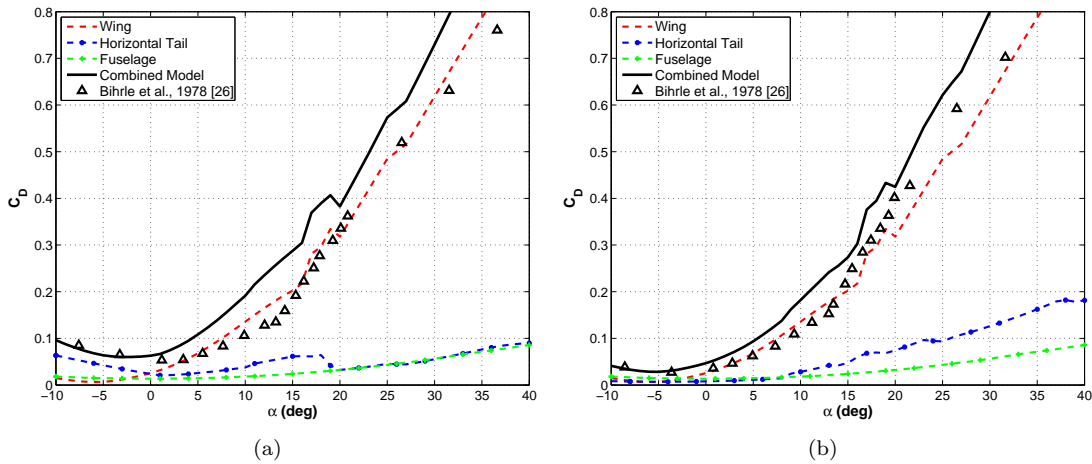
Figure 21. Drag of LWGA fuselage-wing-horizontal tail at Re of 3.45×10^6 at δ_e of (a) -25 deg, (b) 15 deg.

post-stall region, a sharper lift drop is computed as compared with the wind tunnel results.

The drag (Fig. 21) and the moment (Fig. 22) results both follow general trends. The wing drag, however, shows an overprediction in its results which results in an overprediction of the full aircraft drag compared to the wind tunnel data. For the moment, similar order magnitude moments are observed when compared to wind tunnel results. The effects of elevator deflection are clearly observed and is mainly due to the large moment contributions from the horizontal tail.

V.   Conclusions

This paper describes an approach taken to develop a high-fidelity longitudinal aerodynamic model for flight simulation of general aviation aircraft in the stall/post-stall regime. The aerodynamic model used is based on the component-buildup method using strip theory. The aircraft is divided into individual components where for the current study, the fuselage, wing, and horizontal tail are separately modeled. A validated engineering-type procedure was used to model the forces and moments of the fuselage. For the case of the
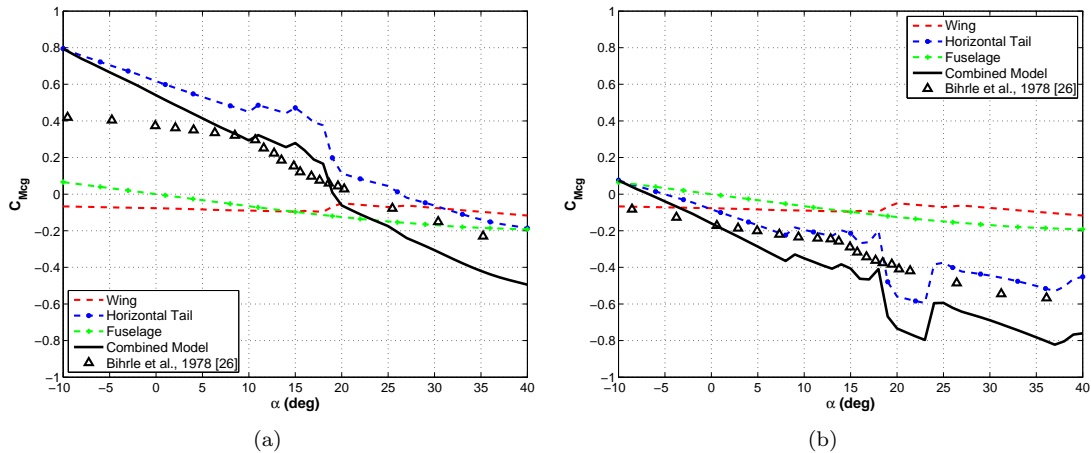
American Institute of Aeronautics and Astronautics

Figure 22. Moment of LWGA fuselage-wing-horizontal tail at Re of 3.45×10^6 at δ_e of (a) -25 deg, (b) 15 deg.

lifting surfaces (wing and horizontal tail), each surface was divided into spanwise panels. An integrated non-linear lifting line theory method was iteratively used to calculate the forces and moments on these surfaces. Each spanwise panel was subject to varying flow characteristics dependent on the aircraft speed and induced flow effects from other components. Aerodynamic data tables based on the airfoil and flap configuration for both the wing and horizontal tail were created to be used by the non-linear lifting line theory method.

The longitudinal aerodynamic modeling approach was validated against wind tunnel test data for a 1/7-scaled single-engine, low-wing general aviation aircraft model that was tested in the 1970/80s as part of the NASA Stall/Spin Project. Numerous configurations that included fuselage only, fuselage-wing only, fuselage-horizontal tail only, fuselage-wing-horizontal tail and finally cases with full aircraft with elevator deflections were modeled and compared against wind tunnel results at a Reynolds number of 3.45×10^6. The validation comparisons clearly indicate that the component-buildup approach using an integrated non-linear lifting line method accurately models the longitudinal aerodynamics of a general aviation aircraft and is able to capture stall and post-stall effects well provided that the aircraft geometry and airfoils used are accurately characterized.

The results also identified a few areas of concern that need to be adressed moving forward. The first area of concern is a more accurate method of modeling the moments generated by the fuselage. The results indicate that the center of lift of the fuselage seems to vary with angle of attack. A proper way of modeling this movement needs to be proposed. Another area of concern is the large drop in lift associated with stall. Wind tunnel results showed a milder stall drop as compared with that computed using the developed model and is related to the method of modeling the post-stall aerdynamics of the airfoil.

References

[1] National Transportation Safety Board Accident Report, "Loss of Control on Approach Colgan Air, Inc. Operating as Continental Connection Flight 3407 Bombardier DHC-8-400, N200WQ Clarence Center, NY," NTBS/AAR 10/01, PB2010-910401, February 2009.

[2] The Bureau of d'Enquetes et d'Analyses (BEA) pour la securite, "Final Report: On the accident on 1 June 2009 to the Airbus A330-203 registered F-GZCP operated by Air France Flight 447 Rio de Janeiro-Paris," Tech. rep., July 2012.

[3] Priest, J., "Research into reduction of Loss-of-Control accident rate in a meaningful and measurable way through the use of innovative pilot training techniques," AIAA Paper 2014-1005, National Harbor, Maryland, January 2014.

[4] Federal Aviation Administration, " QUALIFICATION, SERVICE, AND USE OF CREWMEMBERS AND AIRCRAFT DISPATCHERS," Rules and Regulations 78 FR 67799, November 2013.

[5] ICAO 9625, "Manual of Criteria for the Qualification of Flight Simulation Training Devices," DOC 9625, Montreal, Quebec, Canada, 2009.

[6] International Committee for Aviation Training in Extended Envelopes (ICATEE), "Research and Technology Subcommittee Final Report," Tech. rep., February 28 2013.

[7] Shah, G. H., Cunningham, K., Foster, J. V., Fremaux, C. M., Stewart, E. C., Wilborn, J. E., Gato, W., and Pratt, D. W., "Wind-Tunnel Investigation of Commercial Transport Aircraft Aerodynamics at Extreme Flight Conditions," SAE Technical

American Institute of Aeronautics and Astronautics

Paper 2002-01-2912, Phoenix, Arizona, November 2002.

[8] Cunningham, K., Foster, J. V., Shah, G. H., and Stewart, E. C., "Simulation Study of a Commercial Transport Airplane During Stall and Post-Stall Flight," SAE Technical Paper 2004-01-3100, Reno, Nevada, November 2004.

[9] Foster, J. V., Cunningham, K., Fremaux, C. M., Shah, G. H., Stewart, E. C., Rivers, R. A., Wilborn, J. E., and Gato, W., "Dynamics Modeling and Simulation of Large Transport Airplanes in Upset Condition," AIAA Paper 2005-5933, San Francisco, California, August 2005.

[10] M. M. Murch and J. V. Foster, "Recent NASA Research on Aerodynamic Modeling of Post-Stall and Spin Dynamics of Large Transport Airplanes," AIAA Paper 2007-463, Reno, NV, Jan. 2007.

[11] Murch, A. M., *Aerodynamic Modeling of Post-Stall and Spin Dynamics of Large Transport Airplanes*, Master's thesis, School of Aerospace Engineering, Georgia Institute of Technology, Atlanta, Georgia, August 2007.

[12] Fucke, L., Biryukov, V., Grigorev, M., Rogozin, V., Groen, E., Wentink, M., Field, J., Soemarwoto, B., Abramov, N., Goman, M., and Khrabrov, A., "Developing Scenarios for Research into Upset Recovery Simulation," AIAA Paper 2010-7794, Toronto, Ontario, August 2010.

[13] Abramov, N., Goman, M., Khrabrov, A., Kolesnikov, E., Sidoruk, M., Soemarwoto, B., and Smaili, H., "Aerodynamic Model of Transport Airplane In Extended Envelope for Simulation of Upset Recovery," Paper ICAS 2012-3.1.2, Brisbane, Australia, September 2012.

[14] Groen, E., Ledegang, W., Field, J., Smaili, H., Roza, M., Fucke, L., Nooij, S., Goman, M., Mayrhofer, M., Zaichik, L., Grigoryev, M., and Biyukov, V., "SUPRA Enhanced Upset Recovery Simulation," AIAA Paper 2012-4630, Minneapolis, Minnesota, August 2012.

[15] Abramov, N. B., Goman, M. G., Khrabrov, A. N., Kolesnikov, E. N., Fucke, L., Soemarwoto, B., and Smaili, H., "Pushing Ahead - SUPRA Airplane Model for Upset Recovery," AIAA Paper 2012-4631, Minneapolis, Minnesota, August 2012.

[16] Khrabov, A., Sidoryuk, M., and Goman, M., "Aerodynamic Model Development and Simulation of Airliner Spin for Upset Recovery," *Progress in Flight Physics*, Vol. 5, 2013, pp. 621–636.

[17] Air Safety Institute, "General Aviation Accidents in 2010," 22nd Joseph T. Nall Report, 2013.

[18] National Transportation Safety Board, "Review of U.S. Civil Aviation Accidents: Review of Aircraft Accident Data 2010," NTSB ARA-12/01, Washington D.C, 2010.

[19] National Transportation Safety Board, "NTSB 2015 Most Wanted Transportation Safety Improvements: Prevent Loss of Control In Flight in General Aviation," NTSB Brochure, Washington D.C, 2015.

[20] National Transportation Safety Board, "NTSB 2015 Most Wanted Transportation Safety Improvements: Prevent Loss of Control In Flight in General Aviation," NTSB Brochure, Washington D.C, 2016.

[21] Anonymous, "Partnership to Enhance General Aviation Safety, Accessibility and Sustainability," `https://www.pegasas.aero/`, Accessed Apr. 2016.

[22] Microsoft, "Flight Simulator X," `http://www.fsxworld.com/products/`, Accessed Sep. 2015.

[23] GNU General Public Open Source License, "FlightGear Flight Simulator," `http://www.flightgear.org/`, Accessed Sep. 2015.

[24] Lockheed Martin, "Prepare3D," `http://www.prepar3d.com/`, Accessed Sep. 2015.

[25] Pizkin, S. T. and Levinsky, E. S., "Nonlinear Lifting Line Theory for Predicting Stalling Instabilities on Wings of Moderate Aspect Ratio," Report No. CASD-NCS-76-001, June 1976.

[26] Lutze, F. H. and Lluch, D., "Simulation of stall, spin, and recovery of a general aviation aircraft," AIAA Paper 1996-3409, San Diego, CA, July 1996.

[27] Keller, J. D., McKillip, R. M., Jr., and Wachpress, D. A., "Physical Modeling of Aircraft Upsets for Real-Time Simulation Applications," AIAA Paper 2008-6205, Honolulu, Hawaii, August 2008.

[28] Selig, M. S., "Real-Time Flight Simulation of Highly Maneuverable Unmanned Aerial Vehicles," *Journal of Aircraft*, Vol. 51, No. 6, 2014, pp. 1705–1725.

[29] Selig, M. S., "Modeling Propeller Aerodynamics and Slipstream Effects on Small UAVs in Realtime," AIAA Paper Invited Paper, to be published 8/2/2010, 2010.

[30] Laminar Research, "X-Plane," `http://www.x-plane.com/desktop/home/`, Accessed Sep. 2015.

[31] Paul, R. and Gopalarathnam, A., "Simulation of Flight Dynamics with an Improved Post-Stall Aerodynamics Model," AIAA Paper 2012-4956, August 2012.

[32] Bihrle, W., Jr., Barnhart, B., and Pantason, P., "Static Aerodynamic Characteristics of a Typical Single Engine Low-Wing General Aviation Design for an Angle-of-Attack Range of -8 deg to 90 deg," NASA CR-2971, July 1978.

[33] Bowman, J. S. and Burk, S. M., Jr., "Stall/Spin Research Status Report," Business Aircraft Meeting Report 740354, Wichita, KS, April 1974.

[34] Gloudemans, J. R., Davis, P. C., and Gelhausen, P. A., "A Rapid Geometry Modeler for Conceptual Aircraft," AIAA Paper 96-0052, Reno, NV, Jan. 1996.

[35] Gloudemans, J. R., McDonald, R., Moore, M., Hahn, A., Fredericks, B., and Gary, A., "Open Vehicle Sketch Pad," `http://openvsp.org/`, Accessed Jan. 2015.

[36] Riley, D. R., "Simulator Study of the Stall Departure Characteristics of a Light General Aviation Airplane with or without a Wing-Leading-Edge Modification," NASA TM-86309, May 1985.

[37] Funk Jr., J. D. and McCormick, B. W., "Simulation of Stall Departure using a Nonlinear lifting-line Model," AIAA Paper 91-0340, Reno, NV, Jan. 1991.

[38] Anderson, J. D., Jr., Corda, S., and Van Wie, D. M., "Numerical lifting-line Theory Applied to Drooped Leading-Edge Wings below and above Stall," *Journal of Aircraft*, Vol. 17, No. 12, 1980, pp. 809–904.

[39] Drela, M., "XFOIL: An Analysis and Design System for Low Reynolds Number Airfoils," *Low Reynolds Number Aerodynamics*, edited by T. J. Mueller, Vol. 54 of *Lecture Notes in Engineering*, Springer-Verlag, New York, June 1988, pp. 1–12.

[40]Selig, M. S., Donovan, J. F., and Fraser, D. B., *Airfoils at Low Speeds*, Soartech 8, SoarTech Publications, Virginia Beach, Virginia, 1989.

[41]Selig, M. S., Guglielmo, J. J., Broeren, A. P., and Giguère, P., *Summary of Low-Speed Airfoil Data, Vol. 1*, SoarTech Publications, Virginia Beach, Virginia, 1995.

[42]Selig, M. S., Lyon, C. A., Giguère, P., Ninham, C. N., and Guglielmo, J. J., *Summary of Low-Speed Airfoil Data, Vol. 2*, SoarTech Publications, Virginia Beach, Virginia, 1996.

[43]Lyon, C. A., Broeren, A. P., Giguère, P., Gopalarathnam, A., and Selig, M. S., *Summary of Low-Speed Airfoil Data, Vol. 3*, SoarTech Publications, Virginia Beach, Virginia, 1998.

[44]Selig, M. S. and McGranahan, B. D., "Wind Tunnel Aerodynamic Tests of Six Airfoils for Use on Small Wind Turbines," National Renewable Energy Laboratory, NREL/SR-500-35515, 2004.

[45]Selig, M. S., Deters, R. W., and Williamson, G. A., "Wind Tunnel Testing Airfoils at Low Reynolds Numbers," AIAA Paper 2011-875, January 2011.

[46]Abbott, I. H. and von Doenhoff, A. E., *Theory of Wing Sections, Including a Summary of Airfoil Data*, Dover Books on Aeronautical Engineering Series, Dover Publications, 1959.

[47]Sheldahl, R. E. and Klimas, P. C., "Aerodynamic Characteristics of Seven Airfoil Sections Through 180-Degree of Attack for Use in Aerodynamic Analysis of Vertical Axis Wind Turbines," Sandia National Laboratories, SAND80-2114, Albuquerque, NM, 1981.

[48]Ostowari, C. and Naik, D., "Post-Stall Wind Tunnel Data for NACA 44XX Series Airfoil Sections," SERI/STR-217-2559, January 1985.

[49]Snyder, M. H., Wentz, W. H., and Anwar, A., "Two Dimensional Tests of Four Airfoils at Angles of Attack from 0 to 360 degrees," Wichita State University, Center for Energy Studies, 1981.

[50]Satran, D. and Snyder, M. H., "Two Dimensional Tests of GA(W)-1 and GA(W)-2 Airfoils at Angles-of-Attack from 0 to 360 Degrees," Wichita State University, Center for Energy Studies, 1977.

[51]Rumsey, C., "Overview and Summary of the Second AIAA High-Lift Prediction Workshop," *Journal of the Aircraft*, Vol. 52, No. 4, 2015, pp. 1006–1025.

[52]Coder, J. G. and Maughmer, M. D., "Comparisons of Theoretical Methods for Predicting Airfoil Aerodynamic Characteristics," *Journal of Aircraft*, Vol. 51, No. 1, 2014, pp. 183–191.

[53]Spera, D. A., "Models of Lift and Drag Coefficients of Stalled and Unstalled Airfoils in Wind Turbines and Wind Tunnels," NASA CR-2008-215434, October 2008.

[54]Lindenburg, C., "Stall Coefficients," Energy Research Center of the Netherlands, Petten, ECN-RX-01-004, January 2001, Presented at IEA Symposium on the Aerodynamics of Wind Turbines, National Renewable Energy Laboratory, Golden, CO, December, 2000.

[55]Tangler, J. L. and Ostowari, C., "Horizontal Axis Wind Turbine Post Stall Airfoil Characteristics Synthesization," Presented at the Horizontal-Axis Wind Turbine Technology Conference, Cleveland, OH, May, 1984.

[56]Montgomerie, B., "Methods for Root Effects, Tip Effects and Extending the Angle of Attack Range to ±180 deg, with Application to Aerodynamics for Blades on Wind Turbines and Propellers," FOI-R 1305-SE, Stockholm, Sweeden, June 2004.

[57]Torenbeek, E., *Synthesis of Subsonic Airplane Design*, Springer Science & Business Media, 1982.

[58]McCormick, B. W., *Aerodynamics, Aeronautics, and Flight Mechanics*, John Wiley & Sons, New York, NY, 2nd ed., 1995.

[59]Owens, D. B., "Weissinger's Model of the Nonlinear Lifting-Line Method for Aircraft Design," AIAA Paper 98-0597, Reno, NV, Jan. 1998.

[60]Phillips, W. F. and Snyder, D. O., "Application of Lifting-Line Theory to Systems of Lifting Surfaces," AIAA Paper 2000-0653, Reno, NV, Jan. 2000.

[61]Bertin, J. J., *Aerodynamics for Engineers, Fourth Edition*, Pearson Education, 2006.

[62]Kelley, H. R., "The Estimation of Normal-Force, Drag, and Pitching-Moment Coefficients for Blunt-Based Bodies of Revolution at Large Angles of Attack," *Journal of the Aeronautical Sciences*, Vol. 21, No. 8, 1954, pp. 549–555.

[63]Polhamus, E., "A Review of Some Reynolds Number Effects Related to Bodies at High Angles of Attack," NASA CR-3809, August 1984.

[64]Jorgensen, L. H. and Brownson, J. J., "Effects of Reynolds number and Body Corner Radius on Aerodynamic Characteristics of a Space Shuttle-Type Vehicle at Subsonic Mach Numbers," NASA TN D-6615, Jan. 1972.

[65]Jorgensen, L. H., "A Method for Estimating Static Aerodynamic Characteristics for Slender Bodies of Circular and Noncircular Cross Section Alone and With Lifting Surfaces at Angles of Attack from 0 deg to 90 deg," NASA TN D-7228, April 1973.

[66]Allen, H. J. and Perkins, E. W., "A Study of Effects of Viscosity on Flow over Slender Inclined Bodies of Revolution," NACA TR-1048, Jan. 1951.

[67]Polhamus, E., "Effect of Flow Incidence and Reynolds Number on Low-Speed Aerodynamic Characteristics of Several Noncircular Cylinders with Applications to Directional Stability and Spinning," NASA TN-4176, Jan. 1958.